Jurnal Ilmu Fisika
Vol. 18, No. 2, September 2026, pp. 129–144
ISSN: 1979-4657 (Print); 2614-7386 (Online)
https://doi.org/10.25077/jif.18.2.129-144.2026

Jurnal Ilmu Fisika
Open Access

Eco-Friendly Sol-Gel Synthesis of Silver Nanoparticles using *Morinda citrifolia* Leaf Extract and PVP: Structural, Morphological and Antibacterial Properties

Kiranda Dinata, Shinta Wulan Asih, Lita Rahmasari*

Department of Physics Education, Faculty of Teacher Training and Education, Universitas Sebelas Maret, Jawa Tengah, 57126, Indonesia

Article Info

Article History:

Received December 12, 2025
Revised March 25, 2026
Accepted May 15, 2026
Published online May 20, 2026

Keywords:

Antibacterial
Eco-friendly sol-gel
Morinda citrifolia leaf extract
Polyvinylpyrrolidone
Silver nanoparticles

Corresponding Author:

Lita Rahmasari,
Email: lita@staff.uns.ac.id

ABSTRACT

Silver nanoparticles (AgNPs) have strong potential as antibacterial agents, with effectiveness highly influenced by particle-size stability. This study synthesized AgNPs via a green sol-gel method using noni (Morinda citrifolia) leaf extract as a natural reducing agent and polyvinylpyrrolidone (PVP) as a capping agent. PVP concentrations of 0.5, 1.0, and 1.5 g were mixed with 25 mL noni extract and 25 mL double-distilled water. Characterization using UV–vis, XRD, FE-SEM/EDX, and FTIR showed decreasing UV–vis absorption peaks of 433, 412, 368 nm with increasing PVP content. XRD confirmed a face-centered cubic (FCC) crystal structure with >80% similarity to standard Ag patterns. FE-SEM/EDX indicated the presence of Ag, C, and O elements, and particle sizes remained stable at 16.8, 18.8, and 18.4 nm. The 0.5 g PVP sample produced the smallest particles and showed dominant O–H and C–H functional groups. It exhibited the strongest antibacterial activity, with inhibition zones of 12.5 mm (E. coli) and 12.0 mm (S. aureus). These results demonstrate that eco-friendly sol-gel-synthesized AgNPs using noni leaf extract and PVP exhibit promising antibacterial activity, positioning them as potential candidates for further development as antibacterial materials.

1. INTRODUCTION

The advancement of nanoscience and nanotechnology has revolutionized the utilization of nanomaterials, particularly silver nanoparticles (argentum nanoparticles or AgNPs) (Chen et al., 2023). AgNPs are stable silver particles with diameters ranging from 1–100 nm, renowned for their potent antibacterial properties (More et al., 2023). The primary mechanism of their antibacterial action lies in the release of Ag^+ ions from the AgNPs surface upon contact with bacterial cells. These Ag^+ ions disrupt critical bacterial functions, including membrane integrity, respiratory process, and cellular replication (More et al., 2023; AlQurashi et al., 2025). The antibacterial efficacy of AgNPs is highly dependent on their size. A study by Girma et al. (2024) stated that smaller AgNPs exhibit a larger surface area-to-volume ratio, enabling greater interaction with bacterial cells and thus enhancing their antibacterial activity.

The synthesis method is one of the most critical factors influencing the size of nanoparticles. Generally, AgNPs can be synthesized through three primary approaches: physical, chemical, and biological (Abid et al., 2022). Among these, biological synthesis (or green synthesis) has garnered

significant research attention due to its simplicity, cost-effectiveness, and environmentally friendly reagents (Nethi et al., 2021). In green synthesis, organic materials such as plant extracts serve as key reducing and stabilizing agents, enabling the bottom-up assembly of silver atoms into nanoscale particles.

As a tropical country, Indonesia boasts abundant local flora rich in bioactive compounds, including noni leaves or *Morinda citrifolia* L. (Anas & Yotenka, 2025). Noni leaves have been traditionally recognized for their anti-inflammatory, antifungal, and antimicrobial properties (Chavda et al., 2025). Previous studies have demonstrated that noni leaves contain high concentrations of flavonoids, tannins, and phenolic compounds (Onu, 2024). Based on previous research from Sreelekha et al. (2021) and Vanvalveni et al. (2021). These bioactive constituents serve as natural reducing agents (bioreductors) for Ag^+ ions, facilitating the green synthesis of AgNPs.

Two highly relevant studies have synthesized AgNPs using noni leaf extract as a bioreductor. Akintelu et al. (2021) and Morales-Lozoya et al. (2021) utilized standard green reduction methods, producing AgNPs with diameters of 15–40 nm and 3–27 nm, respectively. However, the particle size ranges reported in these studies remain relatively large and inconsistent. In antibacterial testing, Akintelu et al. achieved inhibition percentages of 20–64%, with the lowest efficacy observed against *Escherichia coli* (E. *coli*). Similarly, Morales-Lozoya et al. evaluated the antibacterial activity of their synthesized AgNPs, demonstrating inhibition zones of 10.6 mm and 9.8 mm against *Staphylococcus aureus* (S. *aureus*) and E. *coli*. The significant variability in particle size and the correspondingly moderate antibacterial activity reported in these studies highlight a critical challenge: the inability of conventional green reduction techniques to produce highly uniform and stable AgNPs with consistently potent antibacterial effects. This lack of size control often leads to particle agglomeration and unpredictable bioactivity, limiting their practical application. To overcome the limitations of conventional reduction, alternative synthesis routes must be explored. The sol-gel technique offers a promising, eco-friendly alternative. It involves a phase transition from a solution (sol) to a gel network, enabling better control over particle nucleation and growth at a relatively low cost and with simple equipment (Badanayak et al., 2021; Bokov et al., 2021). However, as demonstrated by Ratod et al. (2023) and de Souza et al. (2024), the sol-gel method alone can still yield a relatively broad particle size distribution (e.g., 18–75 nm) unless combined with a potent stabilizing agent. Therefore, while sol-gel provides a better foundation, it requires an additional strategy to achieve the monodispersity required for enhanced antibacterial activity.

A widely adopted strategy to overcome the challenge of agglomeration and achieve size-controlled AgNPs is the use of polymeric capping agents, such as polyvinylpyrrolidone (PVP) (Munir et al., 2021; Zein et al., 2022; Neto et al., 2023). PVP is particularly effective due to its amphiphilic nature and cost-effectiveness. As a capping agent, PVP molecules adsorb onto the surface of nascent AgNPs, providing steric stabilization. This mechanism creates a physical barrier that prevents particle aggregation by reducing interparticle van der Waals forces and inhibiting uncontrolled crystal growth (Simsir et al., 2019; Javed et al., 2020). Consequently, PVP facilitates the formation of nanoparticles with a more uniform size and narrower size distribution.

To address these gaps, this study proposes a novel and integrated green synthesis approach. For the first time, to the best of our knowledge, we combine the bioreducing power of Morinda citrifolia (noni) leaf extract with the steric stabilization of polyvinylpyrrolidone (PVP) within an eco-friendly sol-gel framework. We hypothesize that the controlled nucleation environment of the sol-gel process, coupled with the capping action of PVP, will synergistically yield AgNPs with superior size uniformity and colloidal stability compared to conventional green methods. Consequently, these well-defined AgNPs are anticipated to exhibit significantly enhanced and more consistent antibacterial activity, positioning them as promising candidates for biomedical applications.

2. METHOD

2.1 Materials

The materials used in this study were silver nitrate ($AgNO_3$, Merck, ≥98% purity), noni leaf powder (*Morinda citrifolia* L.) obtained from a local herbal plant store in Surakarta, Central Java,

Indonesia, citric acid ($C_6H_8O_6$, Merck, 99% purity), polyvinylpyrrolidone (PVP, K-90 type) as a stabilizing agent, and double-distilled water as the solvent throughout all experiments. All glassware (beakers, volumetric flasks, and stirring rods) were thoroughly washed with ethanol, rinsed with double-distilled water, and subsequently cleaned in an ultrasonic bath for 15 minutes to eliminate any organic or particulate contaminants prior to use.

2.2 Preparation of Noni Leaf Extract

The noni leaf extract was prepared using the powdered leaves. A 7.5 g portion of the powder was weighed and added to 100 mL of double-distilled water in a 250 mL beaker to obtain a 7.5% weight-to-volume (w/v) concentration. The mixture was heated on a hotplate magnetic stirrer at a maximum temperature of 90°C with constant stirring at 300 rpm for 15 minutes. After the extraction process, the mixture was allowed to cool to room temperature. The extract was then filtered through Whatman No. 42 filter paper to remove solid particulates. A 25 mL aliquot of the filtered extract was collected and stored in a sealed container at 4°C for subsequent use in the synthesis. The remaining extract was later characterized using Fourier transform infrared (FTIR) spectroscopy to identify the functional groups responsible for the reduction of silver ions.

2.3 Eco-friendly Synthesis of AgNPs by Sol-gel

The AgNPs were synthesized using an eco-friendly sol-gel method adapted from de Souza et al. (2024) and Riyatun et al. (2023). The synthesis was performed with the following exact mixing sequence and volumes. First, four precursor solutions were prepared: (i) 0.25 M $AgNO_3$ in 100 mL of double-distilled water; (ii) 0.5 M citric acid in 100 mL of double-distilled water; (iii) 25 mL of noni leaf extract prepared; and (iv) three PVP variations (F_1: 0.5 g, F_2: 1.0 g, and F_3: 1.5 g), each dissolved in 25 mL of double-distilled water. Into a 250 mL beaker, 25 mL of $AgNO_3$ solution, 25 mL of citric acid solution, and 25 mL of noni leaf extract were added sequentially and stirred at 300 rpm for 10 minutes. Subsequently, 25 mL of the respective PVP solution was added dropwise into the mixture under continuous stirring at 300 rpm for 15 minutes. The final total volume of the reaction mixture was 100 mL. The mixture was then heated on a hotplate magnetic stirrer at 85°C with constant stirring at 300 rpm. The total reaction time required for gel formation was recorded for each batch. Gelation was consistently observed between 60 to 90 minutes, depending on the PVP concentration. The formation of a gel was confirmed when the mixture ceased to flow upon tilting the beaker.

The pH of the reaction mixture was measured after the addition of all components using a calibrated pH meter (Mettler Toledo). The pH was recorded as (4.5 ± 0.2), and no further pH adjustment was performed to maintain the green chemistry principles of the synthesis.

This procedure was adapted from the methodologies developed by de Souza et al. (2024) and Riyatun et al. (2023). Figure 1 below illustrates the sol-gel procedure performed.

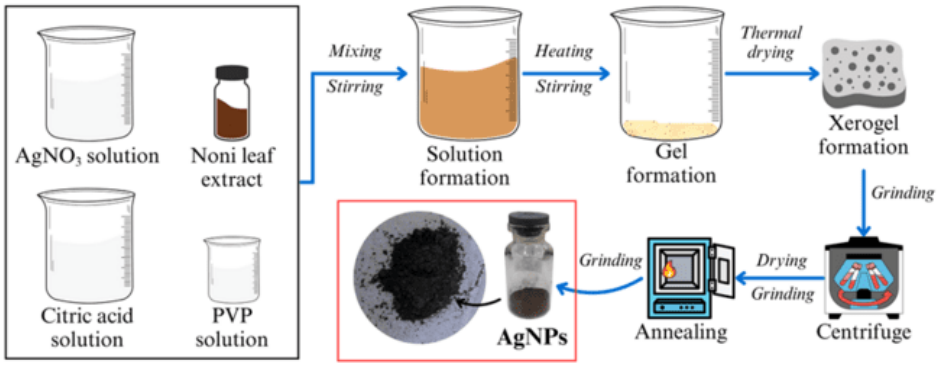

Figure 1 Eco-friendly steps for sol-gel synthesis of AgNPs

2.4 Characterization

The sample characterization was performed using five analytical techniques, including ultraviolet-visible light (UV-vis) spectrophotometry, X-ray diffraction (XRD) spectroscopy, field-emission scanning electron microscopy (FE-SEM), energy-dispersive X-ray (EDX) spectroscopy, and

Fourier transform infrared (FTIR) spectroscopy. The characterization methods are explained in detail below.

2.4.1 UV-vis Spectrophotometry

UV-vis characterization was performed using a Shimadzu UV-1900 Series instrument to measure the absorption of UV-vis light (200–800 nm) by the sample. The generated data was processed using Origin software. This UV-vis analysis served as the preliminary step to confirm the formation of AgNPs (Agustina et al., 2021).

2.4.2 XRD Spectroscopy

Following successful confirmation of AgNPs formation, XRD characterization was conducted using a Bruker D8 Advance instrument to obtain crystallographic information about the formed AgNPs. The data obtained was analyzed in HighScore Plus and Origin software. The data obtained from XRD analysis included diffraction angle (2θ), X-ray intensity, full width at half maximum (FWHM, β), Miller indices (hkl), the percentage of matching silver crystal patterns, interplanar spacing (d), volume (V), surface area (A), surface area-to-volume ratio, and lattice parameter (a). This crystal structure data is essential for determining the crystalline phase and estimating crystallite size. The structural characterization was performed using established methodologies reported by Ali et al. (2023) and Al-Mahmud et al. (2024).

Two basic equations were employed to analyze the structure of the synthesized AgNPs: Debye-Scherrer's law in Equation (1) and Bragg's law in Equation (2). The analysis utilized Cu K-α radiation with a wavelength (λ) of 0.15406 nm, a constant K value of 0.89, and n is the diffraction order (first order =1).

$$D = \frac{K\lambda}{\beta \cos\theta} \tag{1}$$

$$d = \frac{n\lambda}{2 \sin\theta} \tag{2}$$

2.4.3 Electron Microscopy with FE-SEM

FE-SEM characterization was performed using a Jeol IT700HR instrument to examine the sample morphology. The size analysis of AgNPs was performed using ImageJ software by measuring particles from electron microscopy images. The size distribution was plotted as a Gaussian distribution curve using Origin software. Particle counting in ImageJ was repeated twice (or until more than 100 particles were measured) to ensure accurate nanoparticle diameter measurements. The average particle diameter distribution was validated using the R-squared (R^2) value of the Gaussian fit.

2.4.4 EDX Spectroscopy

EDX spectroscopy was employed to determine the elemental composition of the samples. The analysis was conducted under high vacuum conditions with an accelerating voltage of 10 kV and a sample magnification of 10,000 times. Silver or Ag element was typically excited within the energy range of 3.0−3.3 keV (Patil & Chougale, 2021). The EDX spectrometer was integrated with the FE-SEM system as a single analytical unit.

2.4.5 FTIR Spectroscopy

The samples demonstrating the smallest and most stable particle diameters were subsequently analyzed by FTIR using a Shimadzu FT-IR 8201 instrument. The FTIR analysis generated transmittance data in the infrared region, ranging from 4000 to 500 cm^{-1}. The spectral data were processed using Origin software and compared with reference IR absorption data from Mohrig et al. (2010) as well as relevant FTIR results from previous studies.

2.5 Antibacterial Assay

Samples with the smallest diameter and ideal characteristics were selected for testing their antibacterial activity. The disk diffusion method was employed following the Clinical and Laboratory Standards Institute (CLSI) guidelines (2020). The disk diffusion procedure began with the preparation of two agar media using Mueller-Hinton agar (MHA) in petri dishes (90 mm diameter). The MHA media

were inoculated with the Gram-positive bacterium S. aureus and the Gram-negative bacterium E. *coli*. These two bacterial species were chosen as they represent the most common pathogenic microorganisms that infect living organisms, including humans (Rather et al., 2021).

For the test preparation, a colloidal AgNPs solution was prepared by mixing AgNPs powder with dimethyl sulfoxide (DMSO). DMSO solvent was selected as it is non-reactive and can maintain the characteristics of the dissolved AgNPs samples. Filter paper disks (6 mm diameter) were immersed in the colloidal AgNPs solution at concentrations of 50 mg/mL (50%) and 100 mg/mL (100%), along with chloramphenicol antibiotic (positive control) and distilled water (negative control). The disks were then placed on the agar media and incubated for 18 hours at 35°C.

The resulting inhibition zones were measured using a Scan 500 instrument. The inhibition zone percentage of the AgNPs samples was calculated using Equation (3) as follows:

$$IZP = \frac{ZOI}{CIZ} \times 100\% \quad (3)$$

where *IZP* is the inhibition zone percentage, *ZOI* is the zone of inhibition by the sample (mm), and *CIZ* is the positive control inhibition zone (mm).

3. RESULTS AND DISCUSSION

3.1 Extraction and FTIR Study of Noni Leaves

The extraction of noni leaves (*Morinda citrifolia* L.) yielded a dark brown solution with a characteristic herbal aroma. The resulting extract was characterized using FTIR spectroscopy to identify the functional groups responsible for the reduction and stabilization of silver ions during AgNPs synthesis. The FTIR spectrum of the noni leaf extract is presented in Figure 2.

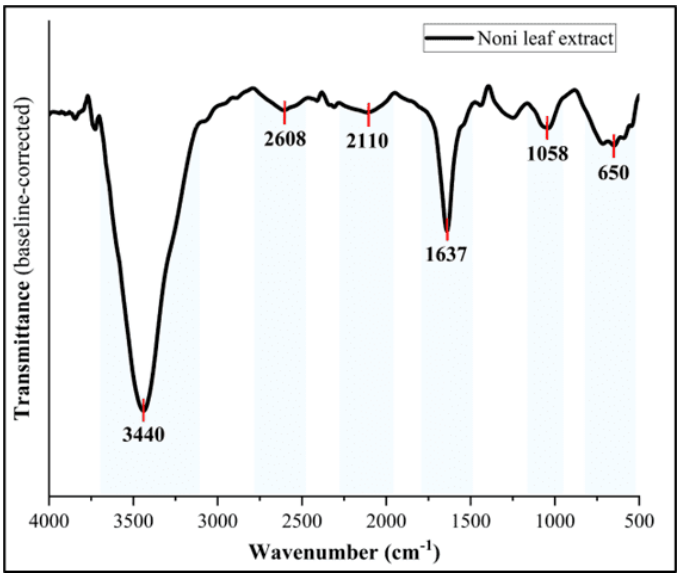

Figure 2 FTIR spectrum of noni leaf extract

The FTIR spectrum exhibited several distinct absorption peaks in the region of 4000–500 cm^{-1}, which are consistent with previous reports on plant-mediated synthesis of nanoparticles (Morales-Lozoya et al., 2021; Nagalingam et al., 2022; Sarkar et al., 2022; Venkatraman et al., 2024). A broad and intense peak was observed at 3440 cm^{-1}, which is attributed to the O–H stretching vibration of hydroxyl groups present in alcohols, phenols, and carboxylic acids (Mohrig et al., 2010; Nandiyanto et al., 2019). This functional group plays a critical role in the reduction mechanism, as the oxygen atoms in hydroxyl groups can donate electrons to reduce Ag^{+} ions to metallic Ag^{0} (AgNPs) (Sarkar et al., 2022).

A sharp peak at 1637 cm^{-1} corresponds to the C=C stretching vibration of aromatic rings or the C=O stretching vibration of amide and carbonyl groups. These functional groups are capable of acting

as both reducing and stabilizing agents; the π-electrons in aromatic systems can participate in electron donation, while carbonyl oxygen atoms can coordinate with silver ions, facilitating nucleation and preventing agglomeration (Vanlalveni et al., 2021; Nagalingam et al., 2022).

Collectively, the FTIR analysis confirms the presence of hydroxyl (–OH), carbonyl (C=O), and aromatic (C=C) functional groups within the noni leaf extract. The hydroxyl and carbonyl groups act as electron donors, facilitating the bioreduction of Ag^+ to Ag^0, and the oxygen-containing groups serve as capping agents, adsorbing onto the nanoparticle surface and providing steric stabilization to prevent particle aggregation (Vanlalveni et al., 2021; Sarkar et al., 2022). These findings establish the potential of noni leaf extract as an effective bioreductant and stabilizer for the eco-friendly synthesis of AgNPs.

3.2 Eco-friendly Sol-gel Forming AgNPs

The solution-to-gel phase requires approximately 2–3 hours of heating on a hotplate stirrer. Controlling the heating time of the sol-gel process is complicated, resulting in variations and differences in the time required for the entire solution to form the gel phase. This process is carried out in an acid chamber with strict temperature control between 80–90°C. The process of heating the solution and forming the gel until oven drying resulted in discoloration of the sample, as shown in Figure 3 below. The observed color change indicates the aggregation process of silver atoms into silver nanoparticles (Arif et al., 2021; Ibrahim et al., 2024).

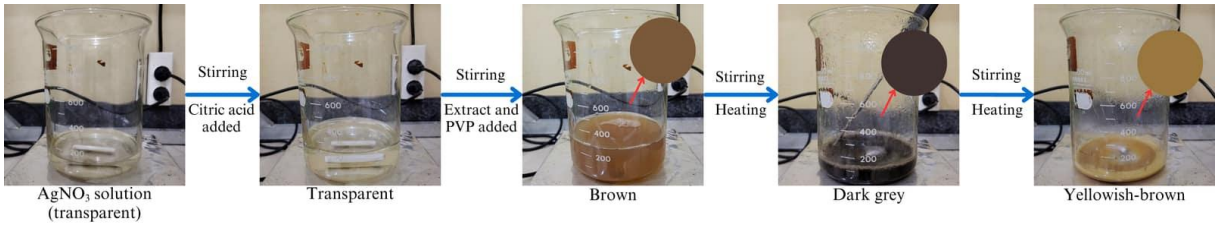

Figure 3 The color of the solution changes from brown to yellowish brown due to heating and gelation

During the synthesis process, the reduction of Ag^+ ions from the precursor solution by noni leaf extract and citric acid was visually confirmed by distinct color changes in the reaction mixture. The nucleation process initiated the formation of AgNPs cores, which were subsequently capped and stabilized by PVP molecules, leading to the formation of stable AgNPs.

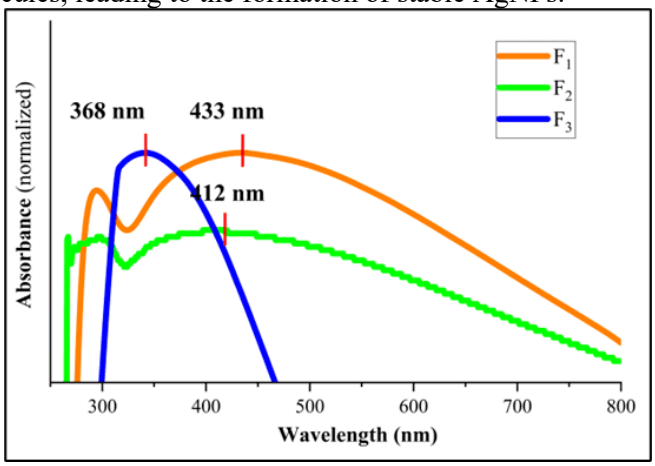

Figure 4 UV-vis absorbance spectrum of AgNPs

3.3 Absorption of UV-vis Spectrum

The formation of AgNPs was initially confirmed through UV-vis spectrophotometry, which detects the characteristic surface plasmon resonance (SPR) phenomenon arising from the collective oscillation of conduction electrons on the nanoparticle surface upon interaction with incident light. The UV-vis absorption spectra of the synthesized AgNPs (F_1, F_2, and F_3) are presented in Figure 4, with corresponding SPR peak wavelengths and absorbance values summarized in Table 1.

UV-vis analysis revealed that higher PVP concentrations in AgNP synthesis resulted in smaller maximum absorption wavelengths (Figure 4 and Table 1). The peak absorption wavelengths ranged from 433 nm (F_1) to 368 nm (F_3), indicating changes in AgNPs size (Yasser & Asfar, 2021). Samples F_1 and F_2 exhibited characteristic AgNPs absorption between 400−500 nm, consistent with previous reports (Khan et al., 2023).

Table 1 Wavelength and absorbance differences for the three samples of AgNPs

Sample	Maximum Wavelength (nm)	Maximum Absorbance (a.u.)
F_1	433	0.209
F_2	412	0.128
F_3	368	1.418

The surface plasmon resonance (SPR) peaks appeared at 350−500 nm, with a dominant peak around 410 nm, typical of small spherical AgNPs (Ider et al., 2017). The presence of a sharp and narrow SPR peak (as observed in F_3 with high absorbance) generally indicates well-dispersed nanoparticles with minimal aggregation (Adrianto et al., 2022). In contrast, broader peaks with lower absorbance (as observed in F_1) may suggest a higher degree of particle aggregation or polydispersity. The blue shift in F_3 may therefore reflect not only smaller particle size but also improved colloidal stability and reduced aggregation, facilitated by the steric stabilization provided by PVP (Bala & Rani, 2020). Smaller AgNPs have a greater surface area, which enhances their antibacterial activity through improved interaction with the bacterial cell wall.

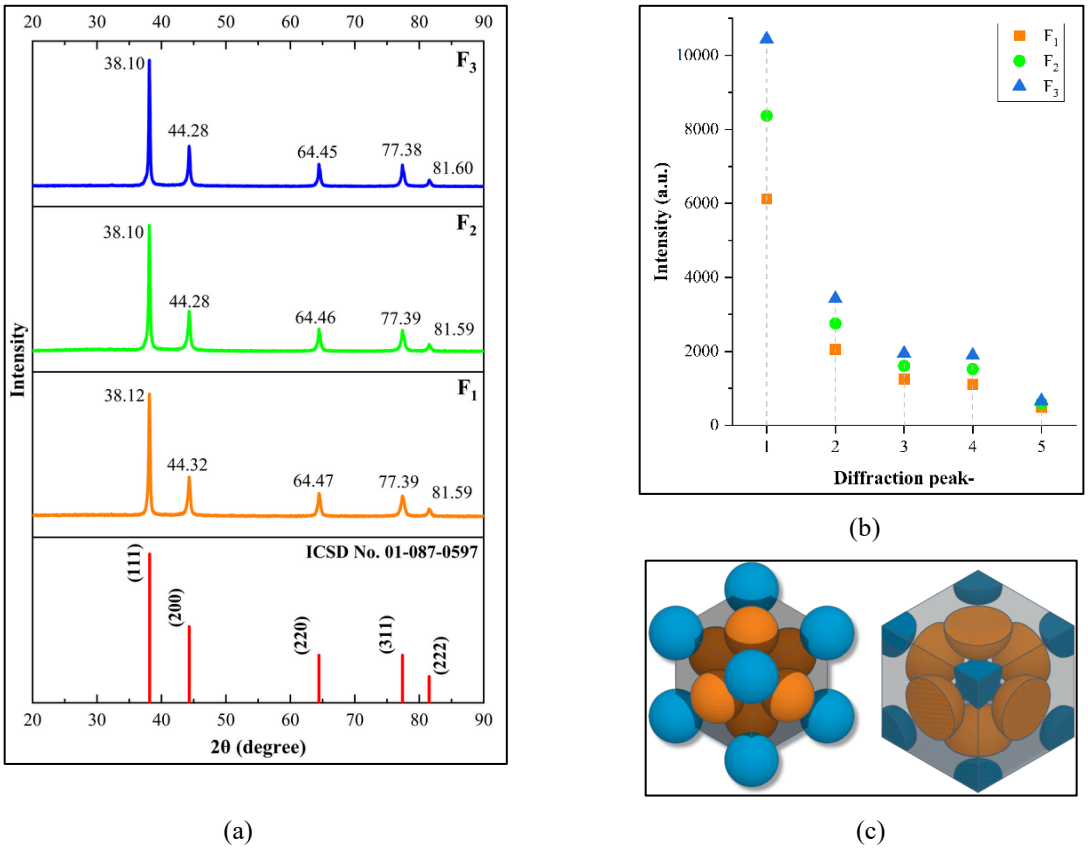

Figure 5 (a) Diffraction angle of XRD graph, (b) X-ray intensity graph at the five XRD peaks, and (c) FCC crystal structure consisting of four atoms per unit cell

It is important to emphasize that the SPR blue shift observed with increasing PVP concentration suggests a trend toward smaller nanoparticle formation, but definitive determination of actual physical particle size requires direct measurement techniques such as FE-SEM or XRD analysis. The UV-vis

data in this study serve as an initial optical confirmation of AgNP formation and provide comparative insight into the relative effects of PVP concentration on the SPR response. The actual crystallite sizes and particle dimensions will be discussed in subsequent sections based on FE-SEM and XRD characterization.

3.4 Crystallographic Structure Analysis

The crystal structure of the synthesized AgNPs was determined through Bragg angle analysis of XRD peak intensities. As shown in Figure 5-a, the XRD patterns of F_1, F_2, and F_3 exhibited diffraction angles consistent with standard silver diffraction patterns (inorganic crystal structure database/ICSD card 01-087-0597). The intensity of diffracted X-rays increases in proportion to the concentration of PVP in the AgNPs sample (Figure 5-b). The percentage of similarity of these patterns is 96%, 86%, and 83%, respectively. All samples crystallized in a face-centered cubic (FCC, Figure 5-c) system with space group Fm-3m (No. 225), characterized by equal lattice parameters ($a = b = c$) and angles ($\alpha = \beta = \gamma = 90°$).

The diffraction patterns revealed identical Miller indices [(111), (200), (220), (311), and (222)] across all variations, aligning with previous reports (Mistry et al., 2021; Patil & Chougale, 2021; Al-Mahmud et al., 2024). Crystallite sizes and interplanar spacing were calculated using Equations (1, 2) (Table 2).

The results showed crystallite diameters of 14.63 nm (F_1), 16.40 nm (F_2), and 18.78 nm (F_3), with incremental size increases of 1.75 nm ($F_1 \rightarrow F_2$) and 2.38 nm ($F_2 \rightarrow F_3$). This positive correlation between PVP concentration and crystallite size suggests that higher PVP concentrations lead to larger nanoparticle crystallites during synthesis. The analysis revealed a proportional increase in both interplanar spacing (0.00001–0.00005 nm) and lattice parameters (0.00002–0.00009 nm), corresponding to the observed expansion of crystallite size. These minute but systematic structural expansions confirm the PVP concentration-dependent lattice strain effects, which can be attributed to surface adsorption of PVP molecules onto the AgNPs surface rather than incorporation into the crystal lattice. The adsorbed PVP layer induces localized strain in the near-surface region of the nanoparticles, resulting in the observed subtle lattice expansion.

Table 2 Interplanar spacing, lattice parameters, and crystallite size from Highscore Plus analysis, Debye-Scherrer's law (Equation (1)), and Bragg's law (Equation (2))

Sample	*d* (nm)	*a* (nm)	*r* (nm)	D_{XRD} (nm)
F_1	0.16513	0.40852	0.14443	14.65
F_2	0.16518	0.40861	0.14447	16.40
F_3	0.16519	0.40863	0.14447	18.78

The surface area values obtained were 674.26 nm^2 (F_1), 844.96 nm^2 (F_2), and 1108.00 nm^2 (F_3) with corresponding crystallite volumes of 1646.31 nm^3, 2309.56 nm^3, and 3468.05 nm^3, respectively. The surface-to-volume ratios decreased progressively with increasing PVP concentration, measuring 4.09×10^8 m^{-1} (F_1), 3.65×10^8 m^{-1} (F_2), and 3.19×10^8 m^{-1} (F_3). The decreasing surface-to-volume ratio indicates a reduction in relative surface exposure as the PVP concentration increases, directly demonstrating PVP's influence on AgNPs crystallite growth.

However, it should be noted that XRD analysis provides information about coherent scattering domains (crystallite size) under the assumption of spherical morphology. Therefore, FE-SEM analysis remains essential for determining the actual morphology, particle size distribution, and degree of agglomeration of AgNPs. This complementary approach will validate whether the observed PVP-dependent trends in crystallite size correspond to changes in actual particle dimensions and will further elucidate the relationship between surface adsorption, microstrain, and particle growth.

3.5 FE-SEM Analysis

The morphology and size distribution of the AgNPs were analyzed using FE-SEM at 100,000 times magnification. Figure 6 presents the corresponding Gaussian-distributed size histograms obtained through ImageJ analysis. The FE-SEM images revealed distinct morphological differences among the

samples: while F_1 and F_3 exhibited well-defined spherical nanoparticles, F_2 showed less distinct shapes with blurred imaging that complicated physical interpretation. The FE-SEM-derived particle diameters were further processed to calculate surface area, volume, and their corresponding ratios, with the quantitative results summarized in Table 3. This analysis provides essential physical parameters for understanding the nanoparticles' potential surface reactivity.

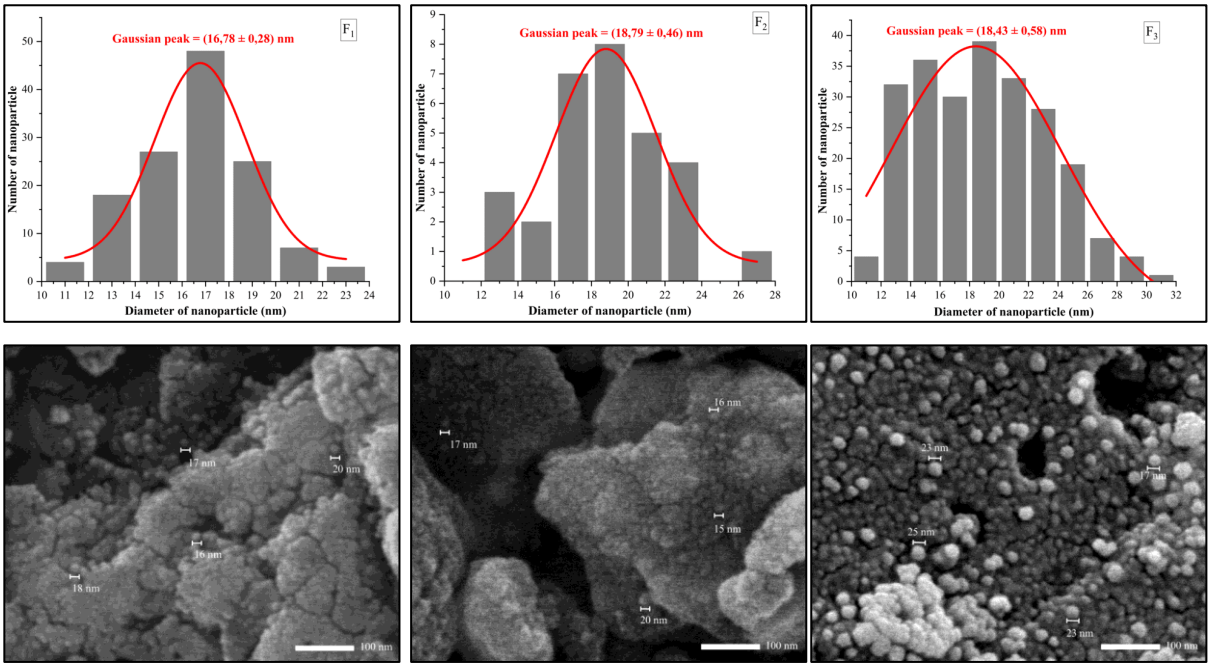

Figure 6 Morphology and size distribution of AgNPs F_1, F_2, and F_3 (left to the right)

Particle size analysis was performed using ImageJ software, where a minimum of 100 particles were measured per sample to ensure statistical significance. Particles with irregular shapes or those overlapping at boundaries were excluded from the measurement to avoid bias. The analysis revealed that the AgNPs in samples F_1, F_2, and F_3 had average diameters of (16.78 ± 0.28) nm, (18.79 ± 0.46) nm, and (18.43 ± 0.58) nm, respectively. The relatively small standard deviations indicate that the size distributions were narrow, particularly for F_1. The R^2 values, ranging from 0.87 to 0.94, demonstrated a good fit to a Gaussian distribution, particularly for sample F_1, which showed the highest correlation.

Table 3 Structural information of AgNPs from FE-SEM analysis with Gaussian distribution and spherical

Sample	$D_{FE\text{-}SEM}$ (nm)	Standard Error (nm)	R^2 Value	Area (A) (nm^2)	Volume (V) (nm^3)	Ratio A/V (m^{-1})
F_1	16.78	0.28	0.94	884.57	2473.86	3.58×10^8
F_2	18.79	0.46	0.87	1109.18	3473.59	3.19×10^8
F_3	18.43	0.58	0.87	1067.09	3277.74	3.26×10^8

The calculation of particle surface area and volume revealed that sample F_1 exhibited the highest A/V ratio (3.58×10^8 m^{-1}), indicating a greater specific surface area compared to samples F2 and F3. This higher A/V ratio, combined with the lower agglomeration percentage observed in F_1, suggests enhanced surface reactivity and better colloidal stability, which may improve the effectiveness of antibacterial applications. It should be noted that the FE-SEM-derived particle diameters (16.78–18.79 nm) are slightly larger than the crystallite sizes obtained from XRD analysis (14.65–18.78 nm), which is expected as FE-SEM measures the physical particle size including any surface coating layer, while XRD measures coherent scattering domain sizes. The difference between these values provides indirect evidence of the presence of a PVP surface layer surrounding the crystalline silver core. Next, a comparison will be made between the FE-SEM results and the XRD results.

3.6 Structure Comparative Analysis of AgNPs from XRD to FE-SEM

The size and stability of AgNPs were assessed through XRD and FE-SEM. These techniques offer complementary but distinct measurements. For well-formed nanoparticles, XRD-derived crystallite sizes often approximate FE-SEM-measured particle sizes, particularly when nanoparticles comprise single crystallites. However, discrepancies emerge in polycrystalline nanoparticles or when surface coatings affect FE-SEM measurements. The combined use of XRD and FE-SEM provides comprehensive nanoparticle characterization, with XRD revealing crystallographic properties and FE-SEM confirming morphology. Table 4 shows a comparison of AgNPs diameters from XRD and FE-SEM studies.

The nanoparticle sizes in this study closely approximated the crystallite dimensions of silver nanocrystals. Size distribution remained stable, with agglomeration observed only in the F_2. The obtained average particle diameters of less than 19 nm yield exceptionally high surface-area-to-volume ratios. These elevated ratios significantly enhance the material's potential for surface-dependent applications, particularly in antibacterial implementations where nanoparticle-bacterial cell interactions are critical. The increased surface availability promotes greater contact efficiency with microbial membranes, thereby improving antimicrobial efficacy.

Table 4 Comparison of crystallite and particle diameters

No.	Reference	Material	D_{XRD} (nm)	$D_{FE\text{-}SEM}$ (nm)
1.	Ali et al. (2023)	AgNPs	20.26	20.63
2.	Basak et al. (2022)	Cobalt ferrite nanoparticles	34.00−37.00	35.00
3.	Mustapha et al. (2021)	Titanium oxide nanoparticles	2.04−4.74	6.80 ± 2.37
4.	This research	AgNPs	14.65 (F_1)	16.78 ± 0.28 (F_1)
			16.40 (F_2)	18.79 ± 0.46 (F_2)
			18.78 (F_3)	18.43 ± 0.58 (F_3)

3.7 Elemental Composition Analysis of AgNPs

EDX detected three primary elements across all samples: silver (Ag), carbon (C), and oxygen (O). It is important to note that EDX analysis provides surface-localized elemental information, with a typical penetration depth of approximately 1–3 μm, depending on the accelerating voltage and sample matrix. Therefore, the reported elemental compositions primarily reflect the surface chemistry of the AgNPs rather than the bulk composition. Figure 7 presents the EDX analysis for the three samples, while Table 5 details the corresponding atomic mass percentages and elemental abundances. EDX analysis revealed distinct elemental distributions among the formulations. Both F_1 and F_2 exhibited Ag atomic percentages exceeding 50% of the total elemental composition. In contrast, F_3 contained only 15% Ag atoms, while demonstrating the highest C content among all samples.

This compositional variation is attributed to the elevated PVP concentration in F_3, which introduced substantial organic carbon components during the synthesis process. The inverse relationship between Ag and C percentages across formulations (F_1/F_2 vs. F_3) indicates that PVP-mediated capping influences both the surface elemental composition and the functional performance of the AgNPs. The thicker PVP coating on F_3, evidenced by its higher carbon content, is expected to significantly affect the release behavior of antibacterial Ag^+ ions. A thicker PVP layer may act as a diffusion barrier, potentially slowing the initial burst release of Ag^+ from the nanoparticle surface while promoting sustained release over a longer period. Conversely, the thinner PVP coating on F_1 and F_2, indicated by lower carbon content, may facilitate more rapid Ag^+ release, which could enhance short-term antibacterial efficacy but may also reduce the longevity of the antibacterial effect. Therefore, the PVP concentration-dependent surface coating thickness represents a critical parameter for tuning the Ag^+ release kinetics and, consequently, the antibacterial performance of the synthesized AgNPs.

Table 5 Composition of elements contained in AgNPs samples

Sample	Percentage of Mass			Percentage of Atom		
	Ag	C	O	Ag	C	O
F_1	89.64	7.18	3.18	51.05	36.74	12.21
F_2	91.66	5.29	2.43	57.99	30.07	10.36
F_3	60.05	32.16	7.79	14.96	71.96	13.08

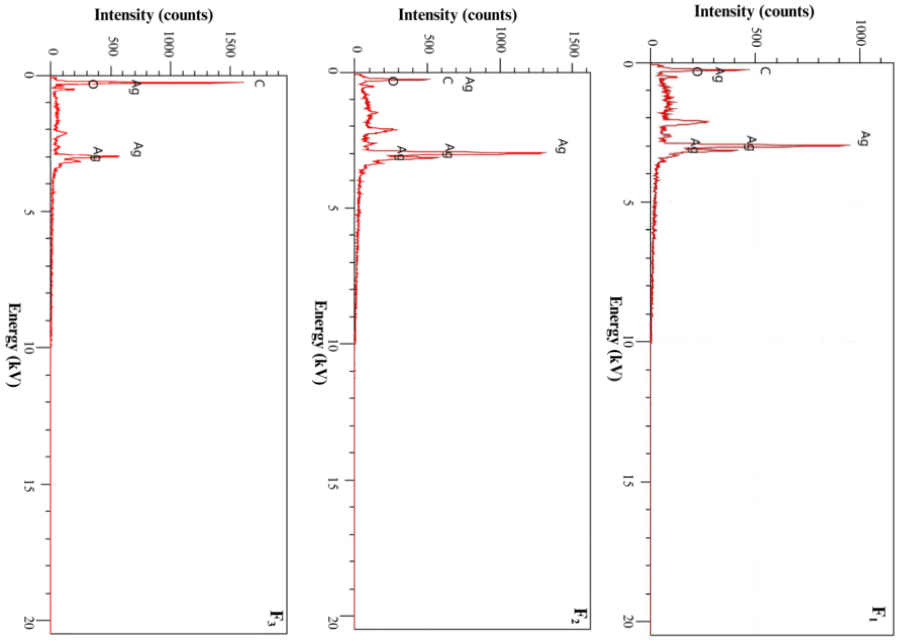

Figure 7 EDX analysis of AgNPs

3.8 FTIR Analysis of AgNPs

The sample exhibiting the strongest antibacterial potential was identified as AgNPs F_1, based on its small particle diameter, low non-silver elemental content, and well-ordered crystalline structure. Further characterization through FTIR spectroscopy revealed the functional groups and chemical bonds present in the F_1 variation, as shown in Figure 8.

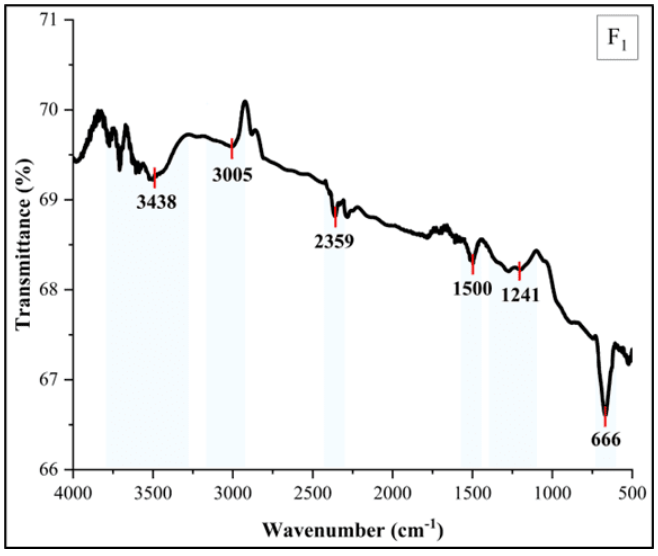

Figure 8 FTIR spectrum of F_1 sample

The FTIR spectrum displayed six distinct transmission minima, with the broadest peak occurring in the single bond region (3800−3300 cm^{-1}). These functional groups and chemical bonds are identified through reference to established spectral databases (Mohrig et al., 2010; Nandiyanto et al., 2019). The analysis confirmed the presence of characteristic groups, including hydroxyl (O−H, 3438 cm^{-1}), alkene/aromatic (C−H, 3005 cm^{-1}), nitrile (C≡N, 2359 cm^{-1}), aromatic ring (C=C−C, 1500 cm^{-1}), ether (−O−, 1241 cm^{-1}), and alkyne (C−H, 666 cm^{-1}). These functional groups (containing C, O, H, and N elements) showed spectral consistency with noni leaf extract peaks at approximately 3400, 1550, and 660 cm^{-1}.

The presence of relatively high amounts of non-silver elements (based on EDX and FTIR) suggests that the noni leaf extract may not only function as a reducing agent but also potentially as a capping agent in conjunction with PVP. This observation indicates the extract's dual role in both the reduction and stabilization processes during nanoparticle synthesis. The next test is the antibacterial assay of sample F_1.

3.9 Antibacterial Activity

The antibacterial evaluation was conducted using the standardized CLSI Kirby-Bauer disk diffusion method. Petri dishes containing MHA, cultures of S. *aureus* and E. *coli*, and AgNPs-impregnated disks were incubated for 18 hours. Figure 9 displays the inhibition zones observed for both bacterial species against the AgNPs samples (specifically F_1) and controls.

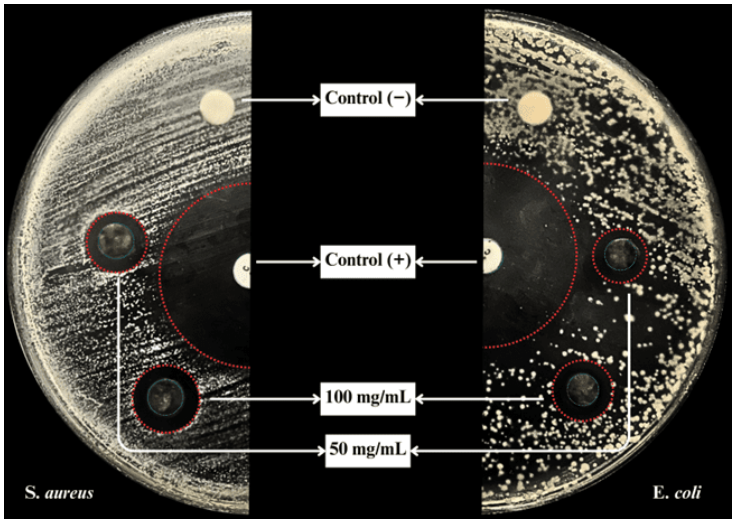

Figure 9 Antibacterial test results of AgNPs using the Kirby-Bauer method

The antibacterial assessment using the disk diffusion method revealed distinct efficacy patterns across studies. Akintelu et al. (2021) tested AgNPs at 25−100 mg/mL concentrations against E. *coli*, demonstrating 20−25% inhibition with streptomycin as a positive control. Morales-Lozoya et al. (2021) employed lower concentrations (2.50−7.50 µg) against both S. *aureus* (10.63 mm inhibition) and E. *coli* (9.81 mm) using ampicillin control. In this research, AgNPs formulation F_1 at 50−100 mg/mL showed stronger activity, producing 11.90−12.50 mm zones (33−34% *IZP*) against S. *aureus* and 11.60−12.00 mm zones (30−31% *IZP*) against E. *coli* with chloramphenicol control.

This superior activity can be correlated with the A/V derived from FE-SEM analysis (Table 3), where F_1 exhibited the highest *A/V* ratio (3.58×10^8 m^{-1}) compared to F_2 (3.19×10^8 m^{-1}) and F_3 (3.26×10^8 m^{-1}). The higher *A/V* ratio of F_1 indicates a greater specific surface area available for interaction with bacterial cell membranes, facilitating more efficient contact and enhanced Ag^+ ion release (More et al., 2023). According to the efficacy criteria established by Putri et al. (2023), where inhibition zones are classified as weak (<5 mm), moderate (5−9 mm), strong (10−19 mm), and very strong (>20 mm), our F_1 AgNPs demonstrated strong antibacterial performance against S. *aureus* and E. *coli*.

AgNPs exhibit multiple interrelated bactericidal mechanisms as described by More et al. (2023) and ALQurashi et al. (2025). The primary mode of action involves the release of Ag^+ ions that interact with bacterial cell membranes, causing structural damage and increased membrane permeability. These ions penetrate bacterial cells, disrupting enzymatic activities and cellular metabolic processes. Additionally, AgNPs generate reactive oxygen species (ROS), inducing oxidative stress that damages DNA, proteins, and other cellular components. According to Menichetti et al. (2023), this bactericidal effect is enhanced by the nanoparticles' large surface area, which facilitates optimal contact with bacterial cells. The nanoscale dimensions of AgNPs enable direct cellular penetration, allowing them to interfere with DNA replication and gene transcription processes. These empirical results highlight the potential of the synthesized AgNPs (particularly F_1) as effective antibacterial agents.

4. CONCLUSION

This study successfully demonstrates the green synthesis of AgNPs using noni (*Morinda citrifolia*) leaf extract via the sol-gel method, with PVP as an effective capping agent. Characterization confirmed the presence of bioactive compounds (tannins, flavonoids) responsible for Ag^+ reduction, while XRD analysis revealed face-centered cubic (FCC) crystalline structures with >80% similarity to standard silver patterns. The inverse relationship between PVP concentration (0.5, 1.0, 1.5 g) and UV-vis absorption (433–368 nm) correlated with particle size, where the 0.5 g PVP formulation (F_1) yielded the smallest AgNPs (crystallite 14.65 nm and FE-SEM 16.78 nm) and exhibited optimal antibacterial activity, evidenced by inhibition zones of 12.5 mm (E. *coli*) and 12.0 mm (S. *aureus*). The sub-19 nm AgNPs showed enhanced antibacterial properties due to their high surface-area-to-volume ratio and functional group composition (C/O/H/N). These findings highlight the potential of PVP-stabilized, green-synthesized AgNPs for medical applications, though further studies should explore broader microbial targets and mechanistic interactions. The sol-gel approach provides a reproducible and environmentally friendly route for producing stable AgNPs.

ACKNOWLEDGEMENT

The authors thank Universitas Sebelas Maret for supporting the Fundamental Research Grant of Universitas Sebelas Maret, with contract number 369/UN27.22/PT.01.03/2025, in 2025.

REFERENCES

Abid, N., Khan, A. M., Shujait, S., Chaudhary, K., Ikram, M., Imran, M., Haider, J., Khan, M., Khan, Q., & Maqbool, M. (2022). Synthesis of nanomaterials using various top-down and bottom-up approaches, influencing factors, advantages, and disadvantages: A review. *Advances in Colloid and Interface Science*, *300*, 102597. https://doi.org/10.1016/j.cis.2021.102597

Adrianto, N., Panre, A. M., Istiqomah, N. I., Riswan, M., Apriliani, F., & Suharyadi, E. (2022). Localized surface plasmon resonance properties of green synthesized silver nanoparticles. *Nano-Structures & Nano-Objects*, *31*, 100895. https://doi.org/10.1016/j.nanoso.2022.100895

Agustina, T. E., Handayani, W., & Imawan, C. (2021). The UV-vis spectrum analysis from silver nanoparticles synthesized using Diospyros maritima blume. leaves extract. *Proceedings of the 3rd KOBI Congress, International and National Conferences (KOBICINC 2020)*, 411–419. https://doi.org/10.2991/absr.k.210621.070

Akintelu, S. A., Folorunso, A. S., Oyebamiji, A. K., & Olugbeko, S. C. (2021). Mosquito repellent and antibacterial efficiency of facile and low-cost silver nanoparticles synthesized using the leaf extract of Morinda citrifolia. *Plasmonics*, *16*(5), 1645–1656. https://doi.org/10.1007/s11468-021-01428-3

Al-Mahmud, M. R., Hossain Shishir, M. K., Ahmed, S., Tabassum, S., Islam Sadia, S., Haque Sachchu, M. M., Tanbin Tama, R., Rahim Miah, A., & Ashraful Alam, M. (2024). Stoichiometry crystallographic phase analysis and crystallinity integration of silver nanoparticles: A rietveld refinement study. *Journal of Crystal Growth*, *643*, 127815. https://doi.org/10.1016/j.jcrysgro.2024.127815

Ali, M. H., Azad, M. A. K., Khan, K. A., Rahman, M. O., Chakma, U., & Kumer, A. (2023). Analysis of crystallographic structures and properties of silver nanoparticles synthesized using PKL extract and nanoscale characterization techniques. *ACS Omega*, *8*(31), 28133–28142. https://doi.org/10.1021/acsomega.3c01261

AlQurashi, D. M., AlQurashi, T. F., Alam, R. I., Shaikh, S., & Tarkistani, M. A. M. (2025). Advanced nanoparticles in combating antibiotic resistance: Current innovations and future directions. *Journal of Nanotheranostics*, *6*(2), 9. https://doi.org/10.3390/jnt6020009

Anas, I. Z., & Yotenka, R. (2025). Analisis cluster luas lahan panen tanaman biofarma di Indonesia tahun 2022. *Emerging Statistics and Data Science Journal*, *3*(1), 485–497. https://doi.org/10.20885/esds.vol3.iss.1.art5

Arif, M. S., Ulfiya, R., Erwin, & Panggabean, A. S. (2021). Synthesis silver nanoparticles using trisodium citrate and development in analysis method. *The 6TH International Conference on Basic Sciences 2020 (ICBS 2020)*, 050007. https://doi.org/10.1063/5.0059493

Badanayak, P., Vastrad, J. V, & Author, C. (2021). Sol-gel process for synthesis of nanoparticles and applications thereof. *The Pharma Innovation Journal*, *10*(8), 1023–1027. http://www.thepharmajournal.com

Bala, A., & Rani, G. (2020). A review on phytosynthesis, affecting factors and characterization techniques of silver nanoparticles designed by green approach. *International Nano Letters*, *10*(3), 159–176. https://doi.org/10.1007/s40089-020-00309-7

Basak, M., Rahman, M. L., Ahmed, M. F., Biswas, B., & Sharmin, N. (2022). The use of X-ray diffraction peak profile analysis to determine the structural parameters of cobalt ferrite nanoparticles using Debye-Scherrer, Williamson-Hall, Halder-Wagner and Size-strain plot: Different precipitating agent approach. *Journal of Alloys and Compounds*, *895*, 162694. https://doi.org/10.1016/j.jallcom.2021.162694

Bokov, D., Turki Jalil, A., Chupradit, S., Suksatan, W., Javed Ansari, M., Shewael, I. H., Valiev, G. H., & Kianfar, E. (2021). Nanomaterial by sol-gel method: Synthesis and application. *Advances in Materials Science and Engineering*, *2021*(1). https://doi.org/10.1155/2021/5102014

Chavda, M., Manani, L., Chandarana, C., & Chavda, P. (2025). A review on noni: Insights into botany, ethnopharmacology, phytochemistry, and commercial prospects. *International Journal of Pharmacognosy*, *12*(2), 100–112. https://doi.org/10.13040/IJPSR.0975-8232.IJP.12(2).100-12

Chen, C., Zhou, H., Ma, Y., Dai, Q., & Tang, Z. (2023). Celebrating 20 years of NCNST: Innovation in nanoscience and nanotechnology. *ACS Nano*. https://doi.org/10.1021/acsnano.3c06711

Clinical and Laboratory Standards Institute (CLSI). (2020). Performance Standards for Antimicrobial Susceptibility Testing. In *Journal of Clinical Microbiology* (30th ed.). CLSI. https://doi.org/10.1128/JCM.01864-19

de Souza, C. C., Ramos, G. Q., Katak, R. de M., Muniz, V. A., Roque, R. A., Ferreira, N. S., Matos, R. S., Xing, Y., & Filho, H. D. F. (2024). Eco-friendly synthesis of silver nanoparticles via Cassava starch: structural analysis and biocidal applications against aedes aegypti and pathogenic bacteria. *Journal of Sol-Gel Science and Technology*. https://doi.org/10.1007/s10971-024-06606-3

Girma, A., Alamnie, G., Bekele, T., Mebratie, G., Mekuye, B., Abera, B., Workineh, D., Tabor, A., & Jufar, D. (2024). Green-synthesised silver nanoparticles: Antibacterial activity and alternative mechanisms of action to combat multidrug-resistant bacterial pathogens: A systematic literature review. *Green Chemistry Letters and Reviews*, *17*(1). https://doi.org/10.1080/17518253.2024.2412601

Ibrahim, N. H., Taha, G. M., Hagaggi, N. S. A., & Moghazy, M. A. (2024). Green synthesis of silver nanoparticles and its environmental sensor ability to some heavy metals. *BMC Chemistry*, *18*(1), 7. https://doi.org/10.1186/s13065-023-01105-y

Ider, M., Abderrafi, K., Eddahbi, A., Ouaskit, S., & Kassiba, A. (2017). Silver metallic nanoparticles with surface plasmon resonance: Synthesis and characterizations. *Journal of Cluster Science*, *28*(3), 1051–1069. https://doi.org/10.1007/s10876-016-1080-1

Javed, R., Zia, M., Naz, S., Aisida, S. O., Ain, N. ul, & Ao, Q. (2020). Role of capping agents in the application of nanoparticles in biomedicine and environmental remediation: Recent trends and future prospects. *Journal of Nanobiotechnology*, *18*(1), 172. https://doi.org/10.1186/s12951-020-00704-4

Khan, M. R., Urmi, M. A., Kamaraj, C., Malafaia, G., Ragavendran, C., & Rahman, M. M. (2023). Green synthesis of silver nanoparticles with its bioactivity, toxicity and environmental applications: A comprehensive literature review. *Environmental Nanotechnology, Monitoring & Management*, *20*, 100872. https://doi.org/10.1016/j.enmm.2023.100872

Menichetti, A., Mavridi-Printezi, A., Mordini, D., & Montalti, M. (2023). Effect of size, shape and surface functionalization on the antibacterial activity of silver nanoparticles. *Journal of Functional Biomaterials*, *14*(5), 244. https://doi.org/10.3390/jfb14050244

Mistry, H., Thakor, R., Patil, C., Trivedi, J., & Bariya, H. (2021). Biogenically proficient synthesis and characterization of silver nanoparticles employing marine procured fungi Aspergillus brunneoviolaceus along with their antibacterial and antioxidative potency. *Biotechnology Letters*, *43*(1), 307–316. https://doi.org/10.1007/s10529-020-03008-7

Mohrig, J. R., Hammond, C. N., & Schatz, P. F. (2010). *Techniques in Organic Chemistry*. Clancy Marshall.

Morales-Lozoya, V., Espinoza-Gómez, H., Z. Flores-López, L., Sotelo-Barrera, E. L., Núñez-Rivera, A., Cadena-Nava, R. D., Alonso-Nuñez, G., & Rivero, I. A. (2021). Study of the effect of the different parts of Morinda citrifolia L. (noni) on the green synthesis of silver nanoparticles and their antibacterial activity. *Applied Surface Science*, *537*, 147855. https://doi.org/10.1016/j.apsusc.2020.147855

More, P. R., Pandit, S., Filippis, A. De, Franci, G., Mijakovic, I., & Galdiero, M. (2023). Silver nanoparticles: Bactericidal and mechanistic approach against drug resistant pathogens. *Microorganisms*, *11*(2), 369. https://doi.org/10.3390/microorganisms11020369

Munir, T., Mahmood, A., Imran, M., Sohail, A., Fakhar-e-Alam, M., Sharif, M., Masood, T., Bajwa, S. Z., Shafiq, F., & Latif, S. (2021). Quantitative analysis of glucose by using (PVP and MA) capped silver

nanoparticles for biosensing applications. *Physica B: Condensed Matter*, *602*, 412564. https://doi.org/10.1016/j.physb.2020.412564

Mustapha, S., Tijani, J. O., Ndamitso, M. M., Abdulkareem, A. S., Shuaib, D. T., Amigun, A. T., & Abubakar, H. L. (2021). Facile synthesis and characterization of TiO2 nanoparticles: X-ray peak profile analysis using Williamson–Hall and Debye–Scherrer methods. *International Nano Letters*, *11*(3), 241–261. https://doi.org/10.1007/s40089-021-00338-w

Nagalingam, M., Rajeshkumar, S., Balu, S. K., Tharani, M., & Arunachalam, K. (2022). Anticancer and antioxidant activity of Morinda citrifolia leaf mediated selenium nanoparticles. *Journal of Nanomaterials*, *2022*(1). https://doi.org/10.1155/2022/2155772

Nandiyanto, A. B. D., Oktiani, R., & Ragadhita, R. (2019). How to read and interpret FTIR spectroscope of organic material. *Indonesian Journal of Science and Technology*, *4*(1), 97. https://doi.org/10.17509/ijost.v4i1.15806

Nethi, S. K., Mukherjee, A., & Mukherjee, S. (2021). Biosynthesized Gold and Silver Nanoparticles in Cancer Theranostics. In *Handbook of Nanomaterials and Nanocomposites for Energy and Environmental Applications* (pp. 759–773). Springer International Publishing. https://doi.org/10.1007/978-3-030-36268-3_29

Neto, F. N. S., Morais, L. A., Gorup, L. F., Ribeiro, L. S., Martins, T. J., Hosida, T. Y., Francatto, P., Barbosa, D. B., Camargo, E. R., & Delbem, A. C. B. (2023). Facile synthesis of PVP-coated silver nanoparticles and evaluation of their physicochemical, antimicrobial and toxic activity. *Colloids and Interfaces*, *7*(4), 66. https://doi.org/10.3390/colloids7040066

Onu, B. U. (2024). Analysis of the phytochemical components of noni (Morinda citrifolia) leaves and stem. *SSRN Electronic Journal*. https://doi.org/10.2139/ssrn.4752639

Patil, R. B., & Chougale, A. D. (2021). Analytical methods for the identification and characterization of silver nanoparticles: A brief review. *Materials Today: Proceedings*, *47*, 5520–5532. https://doi.org/10.1016/j.matpr.2021.03.384

Putri, S. A., Nur Shadrina, A. A., Julaeha, E., & Kurnia, D. (2023). Potential nevadensin from Ocimum basilicum as antibacterial agent against Streptococcus mutans: In vitro and in silico studies. *Combinatorial Chemistry & High Throughput Screening*, *26*(9), 1746–1754. https://doi.org/10.2174/1386207325666220930122813

Rather, M. A., Gupta, K., Bardhan, P., Borah, M., Sarkar, A., Eldiehy, K. S. H., Bhuyan, S., & Mandal, M. (2021). Microbial biofilm: A matter of grave concern for human health and food industry. *Journal of Basic Microbiology*, *61*(5), 380–395. https://doi.org/10.1002/jobm.202000678

Rathod, S. M., Gaikwad, S. V., Gore, S. K., Tumberphale, U. B., Shaikh, S. F., Ubaidullah, M., Pandit, B., & Jadhav, S. S. (2023). Ni–Ag ferrites synthesized by sol gel route using aloe vera extract as a solvent: Enhancement in structural, dielectric, magnetic and optical properties. *Physica B: Condensed Matter*, *661*, 414944. https://doi.org/10.1016/j.physb.2023.414944

Riyatun, R., Kusumaningsih, T., Supriyanto, A., & Purnama, B. (2023). Characteristics of the microstructure, magnetic and antibacterial properties of silver-substituted cobalt ferrite nanoparticles from the sol-gel method. *Kuwait Journal of Science*, *50*(4), 569–574. https://doi.org/10.1016/j.kjs.2023.04.001

Sarkar, B., Bhattacharya, P., Yen Chen, C., Maity, J. P., & Biswas, T. (2022). A comprehensive characterization and therapeutic properties in ripened Noni fruits (Morinda citrifolia L.). *International Journal of Experimental Research and Review*, *29*, 10–32. https://doi.org/10.52756/ijerr.2022.v29.002

Simsir, H., Eltugral, N., & Karagoz, S. (2019). The role of capping agents in the fabrication of nano-silver-decorated hydrothermal carbons. *Journal of Environmental Chemical Engineering*, *7*(5), 103415. https://doi.org/10.1016/j.jece.2019.103415

Sreelekha, E., George, B., Shyam, A., Sajina, N., & Mathew, B. (2021). A comparative study on the synthesis, characterization, and antioxidant activity of green and chemically synthesized silver nanoparticles. *BioNanoScience*, *11*(2), 489–496. https://doi.org/10.1007/s12668-021-00824-7

Vanlalveni, C., Lallianrawna, S., Biswas, A., Selvaraj, M., Changmai, B., & Rokhum, S. L. (2021). Green synthesis of silver nanoparticles using plant extracts and their antimicrobial activities: a review of recent literature. *RSC Advances*, *11*(5), 2804–2837. https://doi.org/10.1039/d0ra09941d

Venkatraman, G., Mohan, P. S., Abdul-Rahman, P. S., Sonsudin, F., Muttiah, B., Hirad, A. H., Alarfaj, A. A., & Wang, S. (2024). Morinda citrifolia leaf assisted synthesis of ZnO decorated Ag bio-nanocomposites for in-vitro cytotoxicity, antimicrobial and anticancer applications. *Bioprocess and Biosystems Engineering*, *47*(8), 1213–1226. https://doi.org/10.1007/s00449-024-02995-5

Yasser, M., & Asfar, A. M. I. A. (2021). Karakterisasi uji kestabilan nanopartikel perak-ekstrak daun sirih hijau menggunakan spektroskopi UV-vis. *Seminar Nasional Penelitian & Pengabdian Kepada Masyarakat (SNP2M)*, 29–32.

Zein, R., Alghoraibi, I., Soukkarieh, C., Ismail, M. T., & Alahmad, A. (2022). Influence of polyvinylpyrrolidone concentration on properties and anti-bacterial activity of green synthesized silver nanoparticles. *Micromachines*, *13*(5), 777. https://doi.org/10.3390/mi13050777